

Image Restoration for Under-Display Camera

Yuqian Zhou¹, David Ren², Neil Emerton³, Sehoon Lim³, and Timothy Large³

¹ University of Illinois at Urbana-Champaign

² University of California, Berkeley

³ Microsoft Corporation

Abstract. The new trend of full-screen devices encourages us to position a camera behind a screen. Removing the bezel and centralizing the camera under the screen brings larger display-to-body ratio and enhances eye contact in video chat, but also causes image degradation. In this paper, we focus on a newly-defined Under-Display Camera (UDC), as a novel real-world single image restoration problem. First, we take a 4k Transparent OLED (T-OLED) and a phone Pentile OLED (P-OLED) and analyze their optical systems to understand the degradation. Second, we design a novel Monitor-Camera Imaging System (MCIS) for easier real pair data acquisition, and a model-based data synthesizing pipeline to generate UDC data only from display pattern and camera measurements. Finally, we resolve the complicated degradation using learning-based methods. Our model demonstrates a real-time high-quality restoration trained with either real or the synthetic data. The presented results and methods provide good practice to apply image restoration to real-world applications.

Keywords: Image Restoration, Denoising, Deblurring, Enhancement, Under-Display Camera

1 Introduction

Under-display Camera (UDC) is a new imaging system that mounts display screen on top of a traditional digital camera lens, as shown in Fig. 1. Such a system has mainly two advantages. First, it follows a new product trend of full-screen devices [11] with larger screen-to-body ratio, which can provide better user perceptive and intelligent experience [12]. Without seeing the bezel and extra buttons, users can easily access more functions by directly touching the screen. Second, it provides better human computer interaction. By putting the camera in the center of the display, it enhances teleconferencing experiences with perfect gaze tracking, and it is increasingly relevant for larger display devices such as laptops and TVs.

Unlike pressure or fingerprint sensors can be more easily integrated into a display, imaging sensor is relatively hard to maintain its functions after being mounted behind a display. The imaging quality of a camera will be severely degraded due to lower light transmission rate and diffraction effects. As a result, images captured will be noisy and blurry. Therefore, while bringing better user

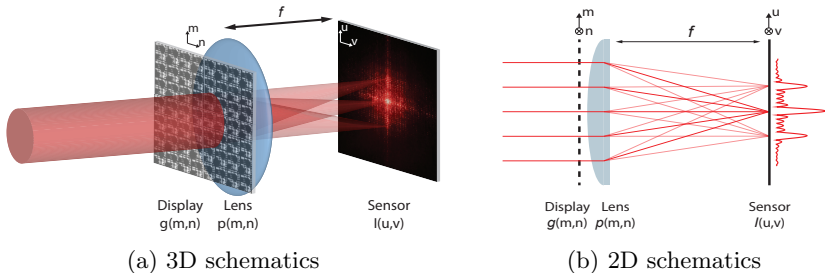


Fig. 1: Under-Display Camera (UDC), a new imaging system that mounts display screen on top of a traditional digital camera lens.

experience and interaction, UDC may sacrifice the quality of photography, face processing and other downstream vision tasks.

Enhancing the degraded images can be better addressed by learning-based image restoration approaches. Recently, deep restoration models have achieved great performance on image processing applications such as de-noising [3, 21, 32, 33, 37, 38], de-blurring [18, 22], de-raining [30, 31], de-hazing [13, 26], super-resolution [19, 28], and light-enhancement [10]. Working on synthesis data with single degradation type, existing models can be hardly utilized to enhance real-world low-quality images with complicated and combined degradation types. To address complicated real degradation using learning-based methods, collecting real paired data or synthesizing near-realistic data by fully understanding the degradation model is necessary.

In this paper, we define and present a novel Under-Display Camera image restoration problem. UDC restoration task is a combination of tasks such as low-light enhancement, de-blurring, and de-noising. Without loss of generality, our analysis focuses on **two types of displays**, a 4K Transparent Organic Light-Emitting Diode (T-OLED) and a phone Pentile OLED (P-OLED), and **a single camera type**, a 2K FLIR RGB Point Grey research camera. We acquire the training data by either collecting real data with a newly proposed data acquisition system, or synthesizing near-realistic data with a model-based pipeline. In summary, we list below our three contributions:

- We define and measure a brand new real-world image degradation type called Under-Display Camera (UDC). It combines various types of image degradation that result from the optical characteristics of the display pattern.
- We propose a novel data acquisition system to collect real paired images, as well as a model-based data synthesis pipeline to generate near-realistic degraded images. The data acquisition and synthesizing methods can be taken as a reference to resolve more real-world image restoration problems.
- We study the potential performance of learning-based methods for the UDC problem, and our promising results show feasibility of high-quality real-time restoration in UDC systems.

2 Real-world Image Restoration

Real-world restoration [3, 36] is becoming a new concept in low-level vision. In the past decades, low-level vision works on synthetic data (denoising on AWGN and SR on Bicubic), but the models are not efficient for images with real degradation such as real noises or arbitrary blur kernels. Making models perform better on real-world inputs usually requires new problem analysis and a more challenging data collection. In the previous literature, there has been two common ways to prepare adaptive training data for real-world problems: real data collection and near-realistic data synthesis.

Recently, more real noise datasets such as DND [24], SIDD [2, 22], and RENOIR [5], have been proposed to address practical denoising problems. Abdelrahman et al. [3] proposed to estimate ground truth from captured smartphone noise images, and utilized the paired data to train and evaluate the real denoising algorithms. In addition to noises, Chen et al. first proposed the SID dataset [10] to resolve extreme low-light imaging. In the area of Single Image Super Resolution (SISR), researchers considered collecting optical zoom data [9, 36] to learn better computational zoom. Other restoration problems including reflection removal [25, 27] also follow the trend of real data acquisition. Collecting real data suffers from limitation of scene variety since most previous models acquire images of postcards, static objects or color boards. In this paper, we propose a novel monitor-camera imaging system, to add real degradation to the existing natural image datasets like DIV2K [4].

Realistic dataset can be synthesized if the degradation model is fully understood and resolved. One good practice of data synthesis is generating real noises on raw sensors or RGB images. CBDNet [16] and Tim et al. [8] synthesized real noises by unfolding the in-camera pipeline, and Abdelhamed et al. [1] better fitted the real noise distribution with flow-based generative models. Zhou et al. [38] adapted the AWGN-RVIN noises into real RGB noises by analyzing the demosaicing process. Other physics-based synthesis was also explored in blur [7] or hazing [6]. For the UDC problem in this paper, we either collected real paired data, or synthesized near-realistic data from model simulation. In particular, we applied the theory of Fourier optics to simulate the diffraction effects, and further adjusted the data with other camera measurements. Our data synthesizing pipeline demonstrates a promising performance for addressing real complicated degradation problem.

3 Formulation

3.1 Optical System Analysis

In this work, we focus on OLED displays [29] as it has superior optical properties compared to traditional LCDs (Liquid Crystal Display). Due to confidentiality reasons it is often difficult to obtain the sample materials used for demos from commercial companies. In this case, we select the displays with different transparencies to improve the generalization. Note that all the displays are **nonactive**

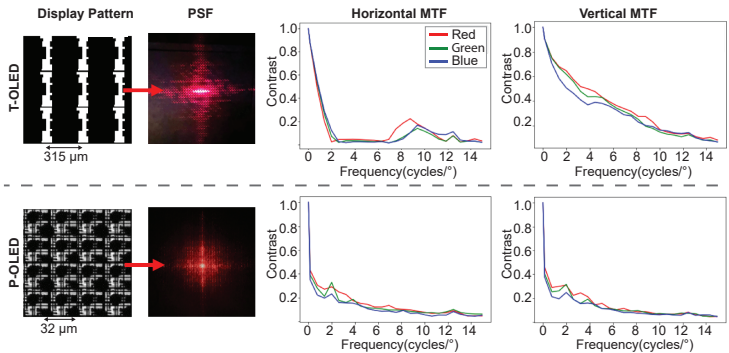


Fig. 2: Optics characteristics of UDC. From left to right: Micrography of display patterns, PSFs (red light only) and MTFs(all Red, green, and blue lights).

Table 1: Comparison of two displays

Metrics	T-OLED	P-OLED
Pixel Layout Type	Stripe	Pentile
Open Area	21%	23%
Transmission Rate	20%	2.9%
Major Degradation	Blur, Noise	Low-light, Color Shift, Noise

in our paper, since in real scenario, the display can be turned off locally when the camera is in operation to 1) reduce unnecessary difficulty from display contents while not affecting user experience and 2) provide users with the status of the device and thus ensure privacy.

Owing to transparent materials being used in OLED display panels, visible lights can be better transmitted through the OLEDs than LCDs. In the meantime, pixels are also arranged such that open area is maximized. In particular, we focus on 4k Transparent organic light-emitting diode (T-OLED) and a phone Pentile OLED (P-OLED). Fig. 2 is a micrograph illustration of the pixel layout in the two types of OLED displays. The structure of the 4K T-OLED has a grating-like pixel layout. P-OLED differs from T-OLED in sub-pixel design. It follows the basic structure of RGBG matrix. In this section, we analyze the two types of displays according to their light transmission rate, point spread function (PSF), and modulation transfer function (MTF).

Light Transmission Rate We measure the transmission efficiency of the OLEDs by using a spectrophotometer and white light source. Table 1 compares the light transmission rate of the two displays. For T-OLED, the open area occupies about 21%, and the light transmission rate is around 20%. For P-OLED, although the open area can be as large as 23%, the light transmission rate is only 2.9%. P-OLED is a flexible/bendable display, which has a poly-amide substrate on which the OLED is formed. Such a substrate may appear yellow in transmis-

sion. Thus, images captured through a polyamide-containing display panel by a UDC may also appear yellow. As a result, imaging through a P-OLED results in lower signal-to-noise ratio (SNR) comparing to using a T-OLED, and has a color shift issue. One real imaging example is shown in Fig. 4.

Diffraction Pattern and Point Spread Function (PSF) Light diffracts as it propagates through obstacles with sizes that are similar to its wavelength. Unfortunately, the size of the openings in the pixel layout is on the order of wavelength of visible light, and images formed will be degraded due to diffraction. Here we characterize our system by measuring the point spread function (PSF). We do so by pointing a collimated red laser beam ($\lambda = 650\text{nm}$) at the display panel and recording the image formed on the sensor, as demonstrated in Fig. 1. Fig. 2 shows the PSFs. An ideal PSF shall resemble a delta function, which then forms a perfect image of the scene. However, light greatly spreads out in UDC. For T-OLED, light spreads mostly across the horizontal direction due to its nearly one dimensional structure in the pixel layout, while for P-OLED, light is more equally distributed as the pixel layout is complex. Therefore, images captured by UDC are either blurry (T-OLED) or hazy (P-OLED).

Modulation Transfer Function (MTF) Modulation Transfer Function (MTF) is another important metric for an imaging system, as it considers the effect of finite lens aperture, lens performance, finite pixel size, noise, non-linearities, quantization (spatial and bit depth), and diffraction in our systems. We characterize the MTF of our systems by recording sinusoidal patterns with increasing frequency in both lateral dimensions, and we report them in Fig. 2. For T-OLED, contrasts along the horizontal direction are mostly lost in the mid-band frequency due to diffraction. This phenomenon is due to the one-dimensional pixel layout of the T-OLED. Fig. 4 shows severe smearing horizontally when putting T-OLED in front of the camera. While for P-OLED, the MTF is almost identical to that of display-free camera, except with severe contrast loss. Fortunately, however, nulls have not been observed in any particular frequencies.

3.2 Image Formation Pipeline

In this section, we derive the image formation process of UDC. In other words, given a calibrated pixel layout and measurements using a specific camera, degraded images can be simulated from a scene. From the forward model, we can synthesize datasets from ground truth images.

Given an object in the scene \mathbf{x} , the degraded observation \mathbf{y} can be modeled by a convolution process,

$$\mathbf{y} = (\gamma\mathbf{x}) \otimes \mathbf{k} + \mathbf{n}, \quad (1)$$

where γ is the intensity scaling factor under the current gain setting and display type, \mathbf{k} is the PSF, and \mathbf{n} is the zero-mean signal-dependent noise. Notice that this is a simple noise model that approximately resembles the combination of

shot noise and readout noise of the camera sensor, and it will be discussed in a later section.

Intensity Scaling Factor (γ) The intensity scaling factor measures the changing ratio of the average pixel values after covering the camera with a display. It simultaneously relates to the physical light transmission rate of the display, as well as the digital gain setting of the camera. γ can be computed from the ratio of δ -gain amplified average intensity values $I_d(\delta, s)$ at position s captured by UDC, to the 0-gain average intensity values $I_{nd}(0, s)$ by naked camera within an enclosed region S . It is represented by,

$$\gamma = \frac{\int_S I_d(\delta, s) ds}{\int_S I_{nd}(0, s) ds} \quad (2)$$

Diffraction Model We approximate the blur kernel \mathbf{k} , which is the Point Spread Function (PSF) of the UDC. As shown in Fig 1, in our model, we assume the display panel is at the principle plane of the lens. We also assume the input light is monochromatic plane wave with wavelength λ (i.e. perfectly coherent), or equivalently light from a distance object with unit amplitude. Let the display pattern represented by transparency with complex amplitude transmittance be $g(m, n)$ at the Cartesian co-ordinate (m, n) , and let the camera aperture/pupil function $p(m, n)$ be 1 if (m, n) lies inside the lens aperture region and 0 otherwise, then the display pattern inside the aperture range $g_p(m, n)$ becomes,

$$g_p(m, n) = g(m, n)p(m, n). \quad (3)$$

At the focal plane of the lens (i.e. 1 focal length away from the principle plane), the image measured is the intensity distribution of the complex field, which is proportional to the Fourier transform of the electric field at the principle plane [15]:

$$I(u, v) \propto \left| \iint_{-\infty}^{\infty} g_p(m, n) \exp \left[-j \frac{2\pi}{\lambda f} (mu + nv) \right] dm dn \right|^2. \quad (4)$$

Suppose $G_p(v_m, v_n) = \mathcal{F}(g_p(m, n))$, where $\mathcal{F}(\cdot)$ is the Fourier transform operator, then

$$I(u, v) \propto |G_p(v_m, v_n)|^2 = \left| G_p \left(\frac{u}{\lambda f}, \frac{v}{\lambda f} \right) \right|^2, \quad (5)$$

which performs proper scaling on the Fourier transform of the display pattern on the focal plane.

Therefore, to compute the PSF \mathbf{k} for image \mathbf{x} , we start from computing Discrete Fourier Transform (DFT) with squared magnitude $M(a, b) = |\hat{G}_p(a, b)|^2$ of the $N \times N$ microscope transmission images \hat{g}_p of the display pattern and re-scaling it. Then, the spatial down-sampling factor r becomes,

$$r = \frac{1}{\lambda f} \cdot \delta_N N \cdot \rho, \quad (6)$$

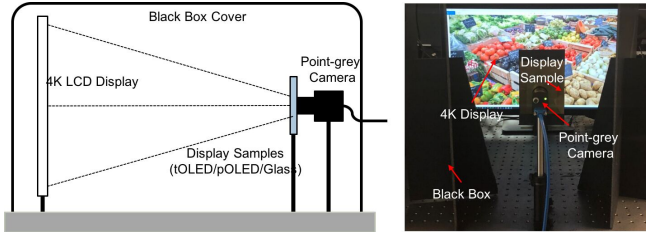


Fig. 3: Monitor-Camera Imaging System (MCIS).

where δ_N is the pixel size of the \hat{g}_p images, and ρ is the pixel size of the sensor. Finally, \mathbf{k} can be represented as

$$k(i, j) = \frac{M_{\downarrow r}(i, j)}{\sum_{(\hat{i}, \hat{j})} M_{\downarrow r}(\hat{i}, \hat{j})}. \quad (7)$$

k is a normalized form since we want to guarantee that it represents the density distribution of the intensity with diffraction effect. Note that only PSF for a single wavelength is computed for simplicity. However, scenes in the real-world are by no means monochromatic. Therefore, in order to calculate an accurate color image from such UDC systems, PSF for multiple wavelengths shall be computed. More details will be shown in Section 4.2.

Adding Noises We follow the commonly used shot-read noise model [8, 17, 20] to represent the real noises on the imaging sensor. Given the dark and blur signal $w = (\gamma \mathbf{x}) \otimes \mathbf{k}$, the shot and readout noises can be modeled by a heteroscedastic Gaussian,

$$\mathbf{n} \sim \mathcal{N}(\mu = 0, \sigma^2 = \lambda_{read} + \lambda_{shot}w), \quad (8)$$

where the variance σ is signal-dependent, and λ_{read} , λ_{shot} are determined by camera sensor and gain values.

4 Data Preparation and Restoration

We propose a novel image acquisition system called Monitor-Camera Imaging System (MCIS). In particular, we display natural images with rich textures on high-resolution monitor and capture them with a static camera. The method is more controllable, efficient, and automatic to capture a variety of scene contents than using mobile set-ups to capture limited static objects or real scenes.

4.1 Monitor-Camera Imaging System

The system architecture is shown in Fig. 3. MCIS consists of a 4K LCD monitor, the 2K FLIR RGB Point-Grey research camera, and a panel that is either

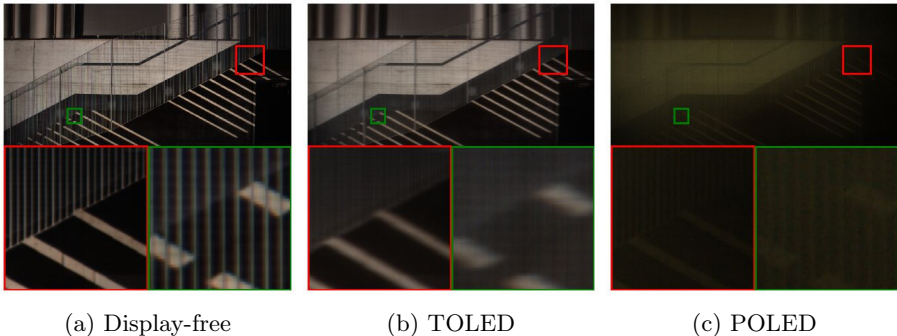


Fig. 4: Real samples collected by the proposed MCIS.

T-OLED, P-OLED or Glass(i.e. no display). The camera is mounted on the center line of the 4K monitor, and adjusted to cover the full monitor range. We calibrate the camera gain by measuring a 256×256 white square shown on the monitor and matching the RGB histogram. For fair comparison and simplicity, we adjust the focus and fix the aperture to f/1.8. It guarantees a reasonable pixel intensity range avoiding saturation while collecting data with zero gain. Suppose we develop a real-time video system, the frame rate has to be higher than 8 fps. So the lowest shutter speed is 125 ms for the better image quality and the higher Signal-to-Noise Ratio (SNR).

We split 300 images from DIV2K dataset [4], and take turns displaying them on a 4K LCD in full screen mode. We either rotate or resize the images to maintain the Aspect Ratio. For training purposes, we capture two sets of images, which are the degraded images $\{y_i\}$, and the degradation-free set $\{x_i\}$.

To capture $\{x_i\}$, we first cover the camera with a thin glass panel which has the same thickness as a display panel. This process allows us to avoid the pixel misalignment issues caused by light refraction inside the panel. To eliminate the image noises in $\{x_i\}$, we average the 16 repeated captured frames. Then we replace the glass with a display panel (T-OLED or P-OLED), calibrate the specific gain value avoiding saturation, and capture $\{y_i\}$. For each set, we record both the 16-bit 1-channel linear RAW CMOS sensor data as well as the 8-bit 3-channel linear RGB data after in-camera pipeline that includes demosaicing. The collected pairs are naturally well spatially-aligned in pixel-level. They can be directly used for training without further transformations.

Due to the yellow substrate inside the P-OLED, certain light colors, especially blue, are filtered out and changes the white balance significantly. We therefore did not further alter the white balance. The light transmission ratio of P-OLED is extremely low, so we set up the gain value to be the maximum (25) for higher signal values. All the detailed camera settings for the two display types are shown in Table 2. One real data sample is shown in Fig. 4

Table 2: Camera Settings for different set of collected data

Parameteres	No-Display	T-OLED	P-OLED
Aperture	f/1.8		
FPS/Shutter	8/125ms		
Brightness	0		
Gamma	1		
Gain	0	6	25(Full)
White-balance	Yes	None	None

Table 3: Measured parameters for data synthesis

Parameteres	T-OLED			P-OLED		
	R	G	B	R	G	B
γ	0.97	0.97	0.97	0.34	0.34	0.20
λ (nm)	640	520	450	640	520	450
r	2.41	2.98	3.44	2.41	2.98	3.44

4.2 Realistic Data Synthesis Pipeline

We follow the image formation pipeline to simulate the degradation on the collected $\{x_i\}$. A model-based data synthesis method will benefit concept understanding and further generalization. Note that all the camera settings are the same as the one while collecting real data. We first transform the 16-bit raw sensor data $\{x_i\}$ into four bayer channels x_r , x_{gr} , x_{gl} , and x_b . Then, we multiply the measured intensity scaling factor γ , compute the normalized and scaled PSF k , and add noises to the synthesize degraded data.

Measuring γ : To measure γ for each channel using the MCIS, we select the region of interest S to be a square region of size 256×256 , and display the intensity value input from 0 to 255 with stride 10 on the monitor. We then record the average intensity both with and without the display for each discrete intensity value, and plot the relationship between display-covered values and no-display-covered ones. Using linear regression, we obtain the ratios of lines for different RRGB channel. For T-OLED, the measured γ is 0.97, same for all the channels. For P-OLED, $\gamma = 0.20$ for the blue channel, and $\gamma = 0.34$ for the other three channels.

Computing PSF: Following equation 3, we acquire the transmission microscope images of the display pattern and crop them with the approximated circular aperture shape with diameter $3333\mu m$, the size of the camera aperture. In equation 6, the $\delta_N N$ is $3333\mu m$. ρ equals to $1.55\mu m/pixel$ in Sony sensor. However, after re-arranging the raw image into 4 RRGB channels, ρ becomes 3.1 for each channel. The focal length for the lens is $f = 6000\mu m$. $\lambda = (640, 520, 450)$ for R, G, B channel, which are the approximated center peaks of the R, G, B filters respectively on the sensor. It yields the down-sampling ratio $r = (2.41, 2.98, 3.44)$ for the R, G and B channels.

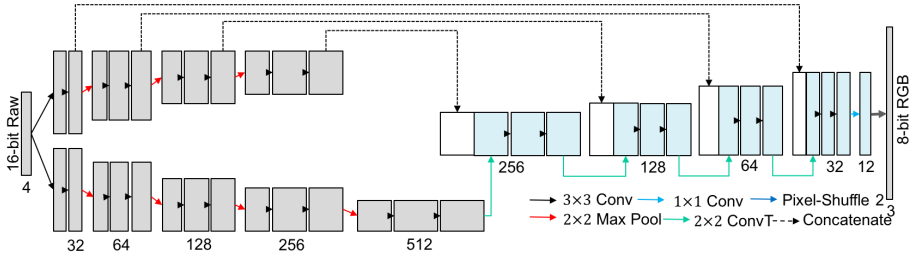


Fig. 5: Network structure. It takes a 4-channel RAW sensor data observation y , and outputs the restored 3-channel RGB image x .

Adding Noises: Finally, we measure λ_{read} and λ_{shot} to estimate the noise statistics. We display random patterns within the 256×256 window on the monitor, collect the paired noisy and noise-free RAW sensor data, and compute their differences. For each of the RRGB channel, we linearly regress the function of noise variance to the intensity value, and obtain the ratio as the shot noise variance, and the y-intersection as the readout noise variance. We then repeat the process for 100 times and collected pairs of data points. Finally, we estimate the distribution and randomly sample λ_{read} and λ_{shot} from it. All the measurements are listed in Table 3.

4.3 Restoration

The proposed restoration network structure is shown in Fig. 5. The proposed model takes a 4-channel RAW sensor data observation y , and outputs the restored 3-channel RGB image x . The model conducts denoising, deblurring, white-balancing, intensity scaling, and demosaicing in a single network, whose structure is basically a UNet. We split the encoder into two sub-encoders, one of which is for computing residual details to add, and the other one learns content encoding from degraded images. By splitting the encoder, compared with doubling the width of each layer, we will have fewer parameters, and make the inference and learning more efficient. To train the model from paired images, we apply the L_1 loss, which will at large guarantee the temporal stability compared with adversarial loss [14]. Besides, we also apply $SSIM$ and Perception Loss (VGG Loss) for ablation study.

5 Experiments

5.1 Implementation

We split the 300 pairs of images in the dataset into 200 for training, 40 for validation and 60 images in the testing partition. Note that all the images have a resolution of 1024×2048 , and we crop patch of 256×256 for training. We crop and augment the training data using the raw image augmentation [21] while

Table 4: Pipeline Comparison

				4K T-OLED		P-OLED	
Pipeline Structure	#P ↓	GFLOPs ↓	T ↓	PSNR/SSIM ↑	LPIPS ↓	PSNR/SSIM ↑	LPIPS ↓
Camera Output	-	-	-	28.83/0.9016	0.3744	15.40/0.6681	0.7590
Wiener Filter [23]	-	-	-	28.50/0.9117	0.4219	16.97/0.7084	0.6306
ResNet-RAW	1.37M	721.76	92.92	36.26/0.9703	0.1214	27.42/0.9176	0.2500
UNet-SynRAW	8.93M	124.36	21.37	32.42/0.9343	0.1739	25.88/0.9006	0.3089
UNet-RAW	8.93M	124.36	21.37	36.71/0.9713	0.1209	30.45/0.9427	0.2219

preserving the RGGB bayer pattern. We train the model using Adam optimizer ($\beta_1 = 0.9$, $\beta_2 = 0.999$ and $\epsilon = 1e - 8$) with learning rate $1e - 4$ and decay factor 0.5 after 200 epochs. We stopped the training at epoch 400, and chose the model with the best validation performance for testing.

5.2 Baseline Methods

We compared our UNet-based method with two baselines:

- **Wiener Filter (WF)** [23]: A general-purpose conventional pipeline concatenating denoising and deconvolution (Wiener Filter), which is an inverse process of the analyzed image formation. To better utilize the unsupervised Wiener Filter (WF) [23], we first apply the BM3D denoiser to each RAW channel separately, afterwards we linearly divide the measured γ with the outputs for intensity scaling. After that, WF is applied to each channel given the pre-computed PSF \mathbf{k} . Finally, RAW images with bayer pattern are demosaiced by linear interpolation.
- **ResNet-RAW**: A data-driven ResNet trained with the same data. To our knowledge, UNet and ResNet-based structures are two widely-used deep models for image restoration. The ResNet-RAW used 16 residual blocks with 64 feature width from EDSR [19]. The model also takes 4-channel RAW data, and outputs 3-channel RGB images.

The above mentioned baselines represent a conventional image processing pipeline and a ResNet-based deep model. Other model variants can be further explored.

5.3 Real Paired Data

The restoration results trained on real paired data are shown in Fig. 6 and 7. The quantitative results are listed in Table 4. We report the performance in PSNR, SSIM, a perceptual metric LPIPS [35], inference time T (ms/MPixels) and GFLOPs. The inference time was tested with one single Titan X, and the GFLOPs is computed by input size of $512 \times 1024 \times 4$. Image deconvolution pipeline introduces many artifacts, and still suffers from the errors of the computed PSF. ResNet-RAW achieves a comparable performance, but it requires more computation operations and longer inference time. The proposed UNet-based structure is efficient and effective, which can therefore be deployed for real-time inference for high-resolution inputs with a single GPU.

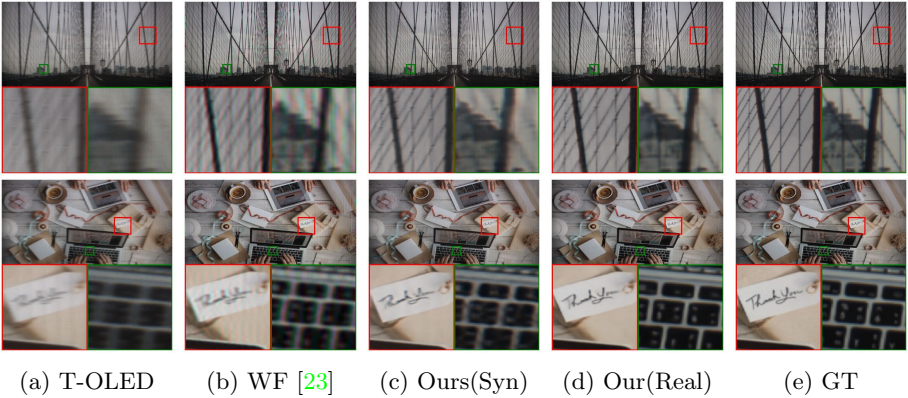


Fig. 6: Restoration Results Comparison for T-OLED. GT: Ground Truth.

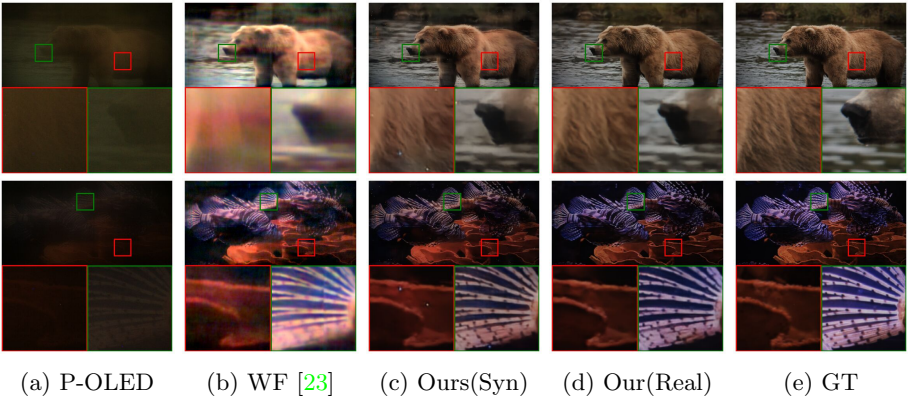


Fig. 7: Restoration Results Comparison for P-OLED. GT: Ground Truth.

5.4 Synthetic Data

We train the same structure using the synthetic data generated by the pipeline proposed in section 4.2, and test the model on real testing partition. In Table 4, we demonstrate that synthetic data still have gaps with the real data, though it has already greatly out-performed the traditional deconvolutional methods for the two display types.

The domain gap mainly comes from the following aspects. First, due to the existing distances between display and lens, in real data there appears visible patterns of the display on the image plane. We recall in the assumption of the diffraction model, the display panel is exactly at the principle plane of the lens system. The cause of the visible bands are illustrated in the supplementary material. Second, the approximated light transmission rate may not be accurate, the measured values may be influenced by other environment light sources. Third, impulse noises caused by dead pixels or over-exposure in the camera sensors



Fig. 8: Face detection performance before and after applying restoration. Without display, the original face recall rate is 60%. Covering the camera with T-OLED or P-OLED will decrease the recall rate to 8% and 0%. After image restoration, the recall rates recovered back to 56% and 39%.

widely exist in the real dataset. Those factors provide more improvement space for the proposed data synthesis model.

5.5 Downstream Applications

The proposed image restoration also enhances the performance of downstream applications including face detection. Fig. 8 shows an example of detecting faces using MTCNN [34]. Without display, the original face recall rate is 60%. Covering the camera with T-OLED or P-OLED will decrease the recall rate to 8% and 0%. After image restoration, the recall rates are recovered to 56% and 39%.

5.6 Ablation Study

Raw Sensor or RGB Data as Inputs Our deep model learns the mapping from 16-bit degraded linear RAW mosaic sensor data (**RAW**) to degradation-free 8-bit 3-channel demosaic RGB data (**RGB**) as in [36]. In this ablation study, **RAW** is replaced by its 8-bit RGB version after in-camera pipeline and **RGB** are not changed. In Table 5, we verified that learning the restoration using RAW-RGB pair is better than using RGB-RGB pair. Our RGB output from the camera is not sRGB colorspace, but it also incorporates bayer pattern demosaicing interpolation compared with RAW. That can be the reason why RAW-RGB pair is better. The 3-channel higher-resolution input RGB also increases the computation operations, resulting in longer inference time.

Table 5: Ablation Study for Camera under 4K T-OLED and P-OLED.

Conditions	4K T-OLED					P-OLED	
	#P ↓	GFLOPs ↓	T ↓	PSNR/SSIM ↑	LPIPS ↓	PSNR/SSIM ↑	LPIPS ↓
Ours	8.93M	124.36	21.37	36.71/0.9713	0.1209	30.45/0.9427	0.2219
RAW → RGB	8.93M	495.60	43.45	35.72/0.9672	0.1428	30.09/0.9377	0.2337
Double Width	31.03M	386.37	40.42	37.00/0.9730	0.1171	30.37/0.9425	0.2044
Single Encoder	7.76M	97.09	15.85	36.47/0.9704	0.1288	30.26/0.9387	0.2318
$L_1 \rightarrow L_1 + SSIM$	8.93M	124.36	21.37	36.69/0.9714	0.1246	30.37/0.9403	0.2131
$L_1 \rightarrow L_1 + VGG$	8.93M	124.36	21.37	36.31/0.9711	0.1130	30.37/0.9403	0.2130

UNet Structure In Table 5, We also compare different UNet structures. We increase the parameter size by splitting the original encoders into two sub-encoders, so the performance is also increased. The increment parameter size and inference time is far less than doubling the width of each layer of UNet, but the performance improvement is comparable (T-OLED), even better (P-OLED). We claim the proposed structure will both maintain a small number of parameters and operations, and achieve a real-time high-quality inference.

Other Losses For more training loss, we add *SSIM* or *VGG* loss in additional to L_1 loss with 1:1 ratio. However, the performance gains on either *SSIM* or perceptual metric LPIPS are not significant enough, and are not visually distinctive. Adversarial loss is not implemented due to its temporal instability compared to GAN-based training. For complicated problems like UDC, training the model solely with L_1 loss is effective enough for good quantitative and qualitative performance.

6 Conclusions

In this paper, we defined and presented a real-world application called under-display camera (UDC). Deploying UDC to full-screen devices improves the user interaction as well as teleconferencing experiences, but does harm to imaging quality and other downstream vision applications. To specifically address the image restoration problem, we systematically analyzed the optical systems and modelled the image formation pipeline of UDC, and both collected real data using a novel acquisition system and synthesized realistic data using optical model. We then proposed a UNet-based network for an efficient real-time high-quality restoration. The model trained with synthetic data also achieved a remarkable performance indicating the potential generalization ability. In all, this paper presented a good practice of applying a learning-based model to UDC and potentially other similar real-world complicated restoration tasks.

References

1. Abdelhamed, A., Brubaker, M.A., Brown, M.S.: Noise flow: Noise modeling with conditional normalizing flows. In: Proceedings of the IEEE International Conference on Computer Vision. pp. 3165–3173 (2019)
2. Abdelhamed, A., Lin, S., Brown, M.S.: A high-quality denoising dataset for smartphone cameras. In: Proceedings of the IEEE Conference on Computer Vision and Pattern Recognition. pp. 1692–1700 (2018)
3. Abdelhamed, A., Timofte, R., Brown, M.S.: Ntire 2019 challenge on real image denoising: Methods and results. In: Proceedings of the IEEE Conference on Computer Vision and Pattern Recognition Workshops. pp. 0–0 (2019)
4. Agustsson, E., Timofte, R.: Ntire 2017 challenge on single image super-resolution: Dataset and study. In: Proceedings of the IEEE Conference on Computer Vision and Pattern Recognition Workshops. pp. 126–135 (2017)
5. Anaya, J., Barbu, A.: Renoir—a dataset for real low-light image noise reduction. *Journal of Visual Communication and Image Representation* **51**, 144–154 (2018)
6. Ancuti, C.O., Ancuti, C., Sbert, M., Timofte, R.: Dense haze: A benchmark for image dehazing with dense-haze and haze-free images. arXiv preprint arXiv:1904.02904 (2019)
7. Brooks, T., Barron, J.T.: Learning to synthesize motion blur. In: Proceedings of the IEEE Conference on Computer Vision and Pattern Recognition. pp. 6840–6848 (2019)
8. Brooks, T., Mildenhall, B., Xue, T., Chen, J., Sharlet, D., Barron, J.T.: Unprocessing images for learned raw denoising. In: Proceedings of the IEEE Conference on Computer Vision and Pattern Recognition. pp. 11036–11045 (2019)
9. Chen, C., Xiong, Z., Tian, X., Zha, Z.J., Wu, F.: Camera lens super-resolution. In: Proceedings of the IEEE Conference on Computer Vision and Pattern Recognition. pp. 1652–1660 (2019)
10. Chen, C., Chen, Q., Xu, J., Koltun, V.: Learning to see in the dark. In: Proceedings of the IEEE Conference on Computer Vision and Pattern Recognition. pp. 3291–3300 (2018)
11. Chen, D.M., Xiong, B., Guo, Z.Y.: Full-screen smartphone (Sep 3 2019), uS Patent App. 29/650,323
12. Evans, V.D.J., Jiang, X., Rubin, A.E., Hershenson, M., Miao, X.: Optical sensors disposed beneath the display of an electronic device (Oct 17 2019), uS Patent App. 16/450,727
13. Fattal, R.: Single image dehazing. *ACM transactions on graphics (TOG)* **27**(3), 72 (2008)
14. Goodfellow, I., Pouget-Abadie, J., Mirza, M., Xu, B., Warde-Farley, D., Ozair, S., Courville, A., Bengio, Y.: Generative adversarial nets. In: *Advances in neural information processing systems*. pp. 2672–2680 (2014)
15. Goodman, J.W.: *Introduction to Fourier optics*. Roberts and Company Publishers (2005)
16. Guo, S., Yan, Z., Zhang, K., Zuo, W., Zhang, L.: Toward convolutional blind denoising of real photographs. In: Proceedings of the IEEE Conference on Computer Vision and Pattern Recognition. pp. 1712–1722 (2019)
17. Hasinoff, S.W.: Photon, poisson noise. *Computer Vision: A Reference Guide* pp. 608–610 (2014)
18. Kupyn, O., Budzan, V., Mykhailych, M., Mishkin, D., Matas, J.: Deblurgan: Blind motion deblurring using conditional adversarial networks. In: Proceedings of the

- IEEE Conference on Computer Vision and Pattern Recognition. pp. 8183–8192 (2018)
19. Lim, B., Son, S., Kim, H., Nah, S., Mu Lee, K.: Enhanced deep residual networks for single image super-resolution. In: Proceedings of the IEEE conference on computer vision and pattern recognition workshops. pp. 136–144 (2017)
 20. Liu, C., Szeliski, R., Kang, S.B., Zitnick, C.L., Freeman, W.T.: Automatic estimation and removal of noise from a single image. *IEEE transactions on pattern analysis and machine intelligence* **30**(2), 299–314 (2007)
 21. Liu, J., Wu, C.H., Wang, Y., Xu, Q., Zhou, Y., Huang, H., Wang, C., Cai, S., Ding, Y., Fan, H., et al.: Learning raw image denoising with bayer pattern unification and bayer preserving augmentation. In: Proceedings of the IEEE Conference on Computer Vision and Pattern Recognition Workshops. pp. 0–0 (2019)
 22. Nah, S., Timofte, R., Baik, S., Hong, S., Moon, G., Son, S., Mu Lee, K.: Ntire 2019 challenge on video deblurring: Methods and results. In: Proceedings of the IEEE Conference on Computer Vision and Pattern Recognition Workshops. pp. 0–0 (2019)
 23. Orieux, F., Giovannelli, J.F., Rodet, T.: Bayesian estimation of regularization and point spread function parameters for wiener–hunt deconvolution. *JOSA A* **27**(7), 1593–1607 (2010)
 24. Plotz, T., Roth, S.: Benchmarking denoising algorithms with real photographs. In: Proceedings of the IEEE Conference on Computer Vision and Pattern Recognition. pp. 1586–1595 (2017)
 25. Punnappurath, A., Brown, M.S.: Reflection removal using a dual-pixel sensor. In: Proceedings of the IEEE Conference on Computer Vision and Pattern Recognition. pp. 1556–1565 (2019)
 26. Ren, W., Liu, S., Zhang, H., Pan, J., Cao, X., Yang, M.H.: Single image dehazing via multi-scale convolutional neural networks. In: European conference on computer vision. pp. 154–169. Springer (2016)
 27. Wan, R., Shi, B., Duan, L.Y., Tan, A.H., Kot, A.C.: Benchmarking single-image reflection removal algorithms. In: Proceedings of the IEEE International Conference on Computer Vision. pp. 3922–3930 (2017)
 28. Wang, X., Yu, K., Wu, S., Gu, J., Liu, Y., Dong, C., Qiao, Y., Change Loy, C.: Esrgan: Enhanced super-resolution generative adversarial networks. In: Proceedings of the European Conference on Computer Vision (ECCV). pp. 0–0 (2018)
 29. Wenke, I.G.: Organic light emitting diode (oled). Research gate (2016)
 30. Zhang, H., Patel, V.M.: Density-aware single image de-raining using a multi-stream dense network. In: Proceedings of the IEEE conference on computer vision and pattern recognition. pp. 695–704 (2018)
 31. Zhang, H., Sindagi, V., Patel, V.M.: Image de-raining using a conditional generative adversarial network. *IEEE transactions on circuits and systems for video technology* (2019)
 32. Zhang, K., Zuo, W., Chen, Y., Meng, D., Zhang, L.: Beyond a gaussian denoiser: Residual learning of deep cnn for image denoising. *IEEE Transactions on Image Processing* **26**(7), 3142–3155 (2017)
 33. Zhang, K., Zuo, W., Zhang, L.: Ffdnet: Toward a fast and flexible solution for cnn-based image denoising. *IEEE Transactions on Image Processing* **27**(9), 4608–4622 (2018)
 34. Zhang, K., Zhang, Z., Li, Z., Qiao, Y.: Joint face detection and alignment using multitask cascaded convolutional networks. *IEEE Signal Processing Letters* **23**(10), 1499–1503 (2016)

35. Zhang, R., Isola, P., Efros, A.A., Shechtman, E., Wang, O.: The unreasonable effectiveness of deep features as a perceptual metric. In: Proceedings of the IEEE Conference on Computer Vision and Pattern Recognition. pp. 586–595 (2018)
36. Zhang, X., Chen, Q., Ng, R., Koltun, V.: Zoom to learn, learn to zoom. In: Proceedings of the IEEE Conference on Computer Vision and Pattern Recognition. pp. 3762–3770 (2019)
37. Zhou, Y., Jiao, J., Huang, H., Wang, J., Huang, T.: Adaptation strategies for applying awgn-based denoiser to realistic noise. In: Proceedings of the AAAI Conference on Artificial Intelligence. vol. 33, pp. 10085–10086 (2019)
38. Zhou, Y., Jiao, J., Huang, H., Wang, Y., Wang, J., Shi, H., Huang, T.: When awgn-based denoiser meets real noises. arXiv preprint arXiv:1904.03485 (2019)